Structure and magnetic properties of Mn/Pt(110)-(1×2): A joint x-ray diffraction and theoretical study

Maurizio De Santis,* Yves Gauthier, and Helio C. N. Tolentino
Institut Néel, UPR 2940-CNRS, 25 Avenue des Martyrs, Boîte Postale 166, 38042 Grenoble, France

Gustav Bihlmayer and Stefan Blügel
Institut für Festkörperforschung, Forschungszentrum, Jülich, D-52425 Jülich, Germany

Véronique Langlais
Institut Néel, UPR 2940-CNRS, 25 Avenue des Martyrs, Boîte Postale 166, 38042 Grenoble, France
and Departament de Fìsica, Universitat Autònoma de Barcelona, Bellaterra, 08193 Barcelona, Spain
(Received 9 March 2007; published 22 May 2007)

The growth of a Mn submonolayer on Pt(110)-(1×2) was studied by surface x-ray diffraction. At room temperature, Mn fills in the empty rows of the clean substrate's missing row structure. At a coverage of 0.5 ML (monolayer), a (1×2) surface alloy is formed, with alternating Pt and Mn dense rows. Upon annealing (or depositing at a substrate temperature of about 570 K), another surface alloy forms with a (2×1) symmetry. It exhibits mixed dense rows where Pt and Mn sites alternate, as in bulk Pt_3Mn. The top layer is corrugated for both the (1×2) and (2×1) surfaces, with Mn lying 0.19±0.03 and 0.16±0.02 Å above the Pt site, respectively. A Pt_3Mn-like slab forms when annealing a 3-ML-thick Mn film. The observed symmetries are at variance with the NiMn and CuMn surfaces where $c(2\times2)$ arrangements were found. Theoretical calculations were performed for (1×2), $c(2\times2)$, and (2×1) PtMn two-dimensional (2D) alloys on Pt(110). Among them, the latter was found to be the ground state. Both the (1×2) and (2×1) surface alloys form antiferromagnetic (AF) Mn chains running in the $[1\bar{1}0]$ and [001] directions, respectively. The ordering within the surface layer switches to ferromagnetic (F) for a 5-ML-thick $Pt_3Mn(110)$ film albeit with a surface structure quite identical to the (2×1) 2D case. The magnetic moment per Mn atom at the surface is close to 4 μ_B, in all cases, among the largest values ever found in similar metal-Mn surface alloys: it is directly related to the surface corrugation and to the Mn volume as already observed for other Mn-based surface alloys. The magnetic order, F or AF, is strongly influenced by the local chemical environment of the Mn sites.

DOI: 10.1103/PhysRevB.75.205432 PACS number(s): 68.55.−a, 75.70.Rf, 61.10.−i

I. INTRODUCTION

Modern techniques (molecular beam epitaxy, e-beam lithography, use of templates, etc.) permit today to elaborate artificial nanostructures based on the peculiar properties of the surface. The synthesis of new structures at a nanometer scale is motivated by the drastic change of the electronic, magnetic, and catalytic properties that often result from reduced dimensionality. The advances in the preparation of magnetic overlayers have allowed the discovery of new phenomena such as giant magnetoresistance and oscillatory magnetic coupling.[1] Properties such as perpendicular magnetic anisotropy and exchange bias are already widely employed in applications.

The surface morphology at the atomic scale has been exploited to elaborate peculiar atomic arrangements aiming at specific applications. An example is the growth of atomic chains of Cu and Ag on vicinal Pt surfaces.[2,3] The impact of low dimensions on the magnetic properties of Co sites was emphasized for atomic chains grown at the steps of Pt(997) vicinal surface.[4] However, vicinal surfaces are not the only morphology providing opportunities to prepare nanowires.

The (110) surfaces of Pt, Au, Ir, and some Pt-metal alloys have in common to exhibit (1×2) or (1×3) missing row reconstructions, with a regular distribution of deep troughs. Such surfaces seem quite attractive to elaborate artificial structures formed by atomic chains of magnetic species, possibly with important catalytic activity, isolated between the surface Pt (Ir, Au) dense rows of the ridge-and-valley structure. For instance, it has been shown that the presence of another metal around the Pt sites provides them with quite special catalytic properties directly connected to the number of neighbors of the other species.[5] Similar mixed distributions, easily reproducible on the nanometer scale at the (110) surface of reconstructed metals or alloys, are likely to modify also the magnetic properties.

Mn shows a large magnetic moment in different metallic environments that motivated extensive studies of thin Mn films on metallic surfaces. Deposition of about half a monolayer (ML) of Mn onto Cu(100),[6] Ni(100),[7,8] Cu(110),[9] and Ni(110) (Ref. 10) results in superstructures with $c(2\times2)$ symmetry. This is a class of two-dimensional (2D) magnetic alloys where Mn atoms occupy substitutional sites in the outermost layer with a checkerboard arrangement. These surface alloys are characterized by a large surface rippling, with Mn atoms shifted outward by 0.2–0.3 Å, which was related to magnetic properties of the surface.[6,9]

Mn is the species that has the largest magnetic moment, 3.64 μ_B (Ref. 11), when forming Pt_3M alloys with $L1_2$ structure, where M is a $3d$ transition metal. Two different phases have been obtained by annealing thick Mn films on Pt(111): a $Pt_3Mn(111)$ alloy with bulklike structure[12] and a surface-

layered ordered alloy made of a regular stacking of $Pt_3Mn(111)$ and Pt(111) layers.[13] A Pt_3Mn-type ordered surface alloy was also obtained by deposition of Mn on Pt(100).[14] These experiments illustrate the trend of Mn to be surrounded by Pt neighbors. Similarly, in the 2D $c(2\times2)$ phases of NiMn and CuMn alloys, the checkerboard ordering yields Mn sites surrounded by the other species.

On the other hand, growth of $L1_0$ PtMn layers, with antiferromagnetic order and high Néel temperature, is very interesting in applications. PtMn is used in spin valves for high-density recording and the degree of chemical order is the critical parameter to reduce the film thickness.[15]

Owing to its larger lattice parameter and to its missing row structure, Pt(110) may yield quite different an environment to the Mn species and result in even more interesting magnetic behaviors at variance with those observed when alloyed with Ni and Cu. This trend shows up in the chemical ordering of the PtMn surface alloys that differ from those of the NiMn and CuMn alloys. This is why Pt was considered in the present study. In the following, we report on two different structures of surface PtMn alloys obtained by deposition of 0.5 ML of Mn on Pt(110)-(1×2). Different elaboration conditions allow to prepare similar surface compositions associated to (1×2) periodicity (RT as deposited film) or to (2×1) symmetry (annealing of the previous film). In none of these cases a $c(2\times2)$ phase was observed.

To substantiate these findings and to examine also the magnetic structure of the observed surface alloys, we performed calculations based on the density-functional theory (DFT), using our quantitative x-ray diffraction (XRD) analysis as input to the *ab initio* calculations. A comparison of the total energies of the (1×2), (2×1), and $c(2\times2)$ structures indicates that the former is kinetically stabilized against formation of a (2×1) alloy, while the latter structure is only metastable. These surface structures are compared to a bulk-like alloy, prepared by annealing a 3 ML Mn film, on a structural as well as magnetic point of view. Antiferromagnetic Mn chains form on the surface of Pt(110), while in thicker Pt_3Mn films a ferromagnetic surface alloy is favored.

II. XRD RESULTS

A. Experimental setup

The experiment was performed at the European Synchrotron Radiation Facility (ESRF) (BM32 beam line). The x-ray source is a bending magnet and the monochromator is a Si(111) double crystal, with the second crystal bent to give sagittal focusing on the sample. The vertical focusing is provided by a mirror, resulting in a spot size of about 0.5×0.3 mm^2. The measurements were performed at photon energy of 18 keV, with an energy resolution of 4 eV.

The experimental station consists of an ultrahigh vacuum chamber fully equipped for sample preparation, mounted on a *Z*-axis diffractometer. Further degrees of freedom are available to align the sample. A full description is given elsewhere.[16]

The Pt(110) single crystal offers a 10-mm-diameter surface with a mosaic spread lower than 0.05°. However, a crystallite covering about 1/5 of the surface and rotated in plane by 0.25° was observed. The sample was cleaned by repeated cycles of Ar^+-ion sputtering and annealing at about 1100 K. The substrate temperature was measured using an infrared pyrometer. At intermediate stages, a 10 min annealing at 900 K in 5×10^{-6} mbar O_2 was also performed to reduce C contamination below the Auger detection level. The surface showed then a sharp (1×2) reconstruction. The average terraces and domain sizes for clean and Mn-covered surfaces were evaluated from the width of transverse scans through the crystal truncation rods close to antiphase conditions and superstructure rods, respectively.[17]

Manganese was evaporated from an effusion cell with an alumina crucible heated at 973 K. The base pressure in the chamber was in the low 10^{-11} mbar range, rising up to $\sim2\times10^{-10}$ mbar during evaporation. The deposition rate, about 1 ML in 12 min, was calibrated with a quartz microbalance and cross-checked measuring the XRD intensity maximum during deposition at a well-defined (*HKL*) reflection.

Data were collected at a grazing incidence angle of 1°. A unit cell was chosen to index the reflections with $\mathbf{A}_1$ and $\mathbf{A}_2$ in the surface plane and $\mathbf{A}_3$ perpendicular to it: $\mathbf{A}_1=(a_{Pt}/2)\times[1\bar{1}0]$, $\mathbf{A}_2=a_{Pt}\times[001]$, and $\mathbf{A}_3=(a_{Pt}/2)\times[110]$ (a_{Pt} being the bulk lattice constant of Pt).

B. Film growth and data collection

The real-time measurement of a surface reflection during Mn deposition shows that, at room temperature, the (1×2) reconstruction disappears beyond ~1 ML. Meanwhile, the intensity of (111) reflection, which is close to the antiphase condition for bulk Pt, shows a maximum at ~0.5 ML. Since this reflection is very sensitive to surface roughness,[17] this maximum was interpreted as the completion of the missing rows of the substrate: it was used to refine the Mn deposition rate obtained by the microbalance. A new surface was prepared according to this calibration and the shutter was closed when the (111) intensity reached its maximum. Sharp (1×2) reconstruction peaks are then present and this structure will be referred to in the following as the Pt(110)-(1×2)Mn surface. This superstructure quickly disappears when the sample is gently annealed (well below 450 K, the lower limit of our pyrometer).

A freshly prepared surface, with 1 ML Mn, was annealed at increasing temperatures. A (2×1) superstructure appeared beyond ~560 K and improved up to 620 K. The same pattern was obtained by depositing Mn on the clean Pt(110)-(1×2) kept at different temperatures in the range $540<T_S<620$ K. The intensity of a strong noninteger reflection, the (1/2 0 0.55), was monitored during growth. The (2×1) structure appears only after 4 min, 30 s and the signal goes through a maximum—considered as corresponding to completion of the surface alloy layer—at ~7 min, 30 s (i.e., about 0.37 and 0.62 ML, respectively). Then, a fresh surface was elaborated for the quantitative analysis by evaporating 0.62 ML Mn at $T_S=570$ K, and subsequent annealing at 650 K. This will be referred to as Pt(110)-(2×1)Mn-2D from now on.

Finally, for a better understanding of the (2×1) superstructure, 3 ML of Mn were deposited on the clean substrate and annealed at 790 K. This yields a (2×1) phase, too, referred as Pt(110)-(2×1)Mn-three-dimensional (3D).

These four surfaces, i.e., (a) Pt(110)-(1×2), (b) Pt(110)-(1×2)Mn, (c) Pt(110)-(2×1)Mn-2D, and (d) Pt(110)-(2×1)Mn-3D, were studied quantitatively. Complete sets of reflections along integer and noninteger rods were measured for each of them. At each (HKL) node, the reflection was measured by rocking the sample around the surface normal. Then, the intensity was integrated numerically, with the exception of the (2×1) superstructure reflections of (c) and (d), whose line shape and width allow for Lorentzian and Gaussian fits, respectively. Structure factors were extracted applying standard correction factors[18] and symmetry ($p2mm$) averaging. Error bars for the structure factors were based on the agreement factor[19] between equivalent reflections. A total of 139 (184), 364 (717), 222 (426), and 101 (119) nonequivalent (total) reflections with average agreement factors of 0.029, 0.051, 0.054, and 0.055 were measured for the (a), (b), (c), and (d) cases, respectively. The (0 3/2 0.15) and (1/2 0 0.55) structure factors, periodically monitored during collection of data set (b) and (c), respectively, decreased by less than 10% (the former) and 15% (the latter) during acquisition. The experimental structure factors for Pt(110)-(1×2)Mn, Pt(110)-(2×1)Mn-2D, and Pt(110)-(2×1)Mn-3D are shown in Figs. 1–3.

The clean Pt(110) surface showed a sharp (1×2) reconstruction with average terraces larger than 230 nm along $\mathbf{A}_1$ (surface rows direction) and about 45 nm along $\mathbf{A}_2$ ([001]), as shown by the (0 1/2) rod and (1 0) crystal truncation rod (CTR).

We note that the average terrace size does not change when evaporating Mn to produce the metastable Pt(110)-(1×2)Mn phase. This is a clear evidence that Mn deposition does not modify the morphology, i.e., no long-range transport occurs.

The situation is different for Pt(110)-(2×1)Mn-2D since, either starting from the (1×2) phase or by evaporation on a hot sample, alloying along the dense rows requires diffusion (albeit over short distances) so that antiphase walls and steps are likely to occur. We actually find smaller domains, 30×15 nm^2, on the average. For the 3D alloy, terraces have similar dimensions, 20×20 nm^2, as derived from the CTR width, but the correlation length associated to the chemical order reduces to about 6 nm on average.

The detector slits were adjusted to yield resolutions of about 9 and 6 nm for the (1×2) and (2×1) superstructures, respectively. As a consequence, for the 3D alloy, the superstructure rods are not fully integrated along Q longitudinal direction, and about 70% only of the intensity is collected.[20]

The four structures were determined via a fit of the simulated structure factors to the experimental ones and a χ^2 minimization. In Tables I and II, the R factor ($R=\Sigma||F|_{\text{expt.}}-|F|_{th}|/\Sigma|F|_{\text{expt.}}$) is also given for comparison. Both structure factors extraction and surface parameter fitting were performed using the ANA-ROD package.[21]

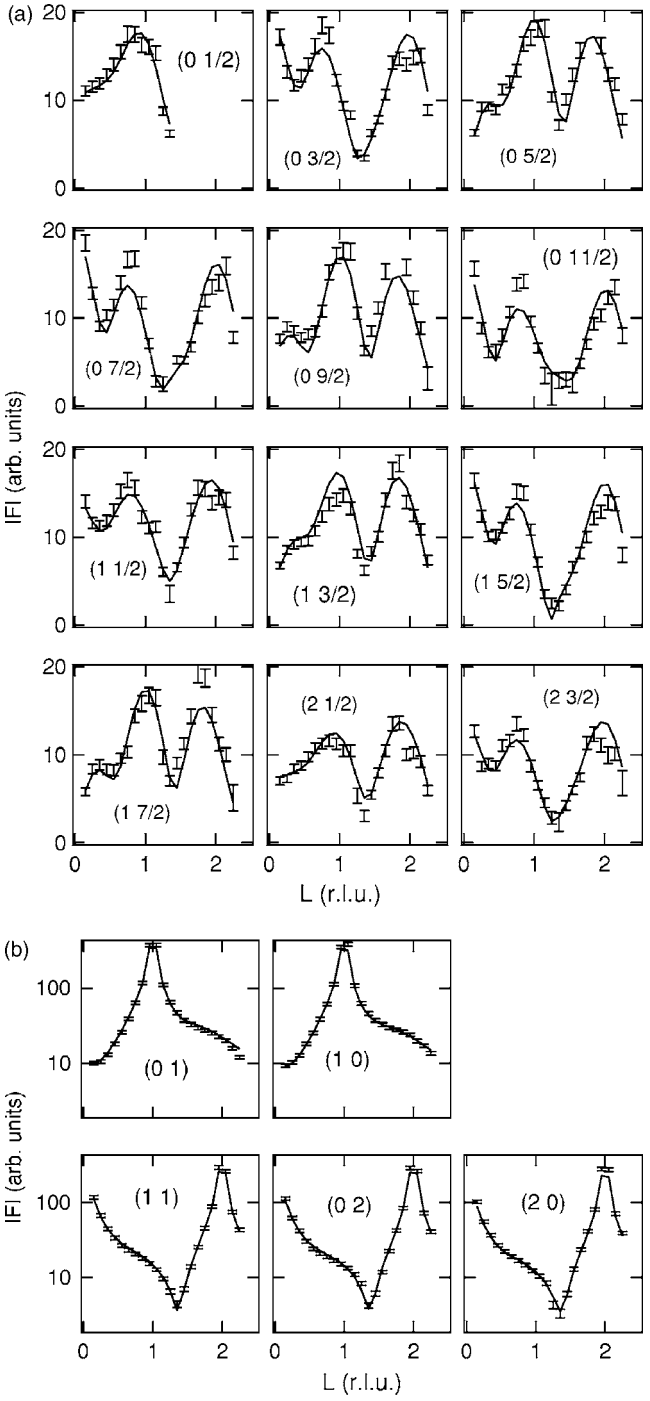

FIG. 1. Experimental structure factors of noninteger rods (a) and CTRs (b) for Pt(110)-(1×2)Mn. They are compared to the best fit (continuous line).

C. Structural analysis

1. Pt(110)-(1×2)

The clean Pt structure was fitted first for reference. The parameters for this well-known missing row model are indicated in Fig. 4(a) (white atoms only). Three interlayer distances, the third layer buckling (b_3), and pairing along the [001] direction in the second (p_2) and fourth (p_4) layers were considered. d_{ij} represents the interlayer spacing from layer i

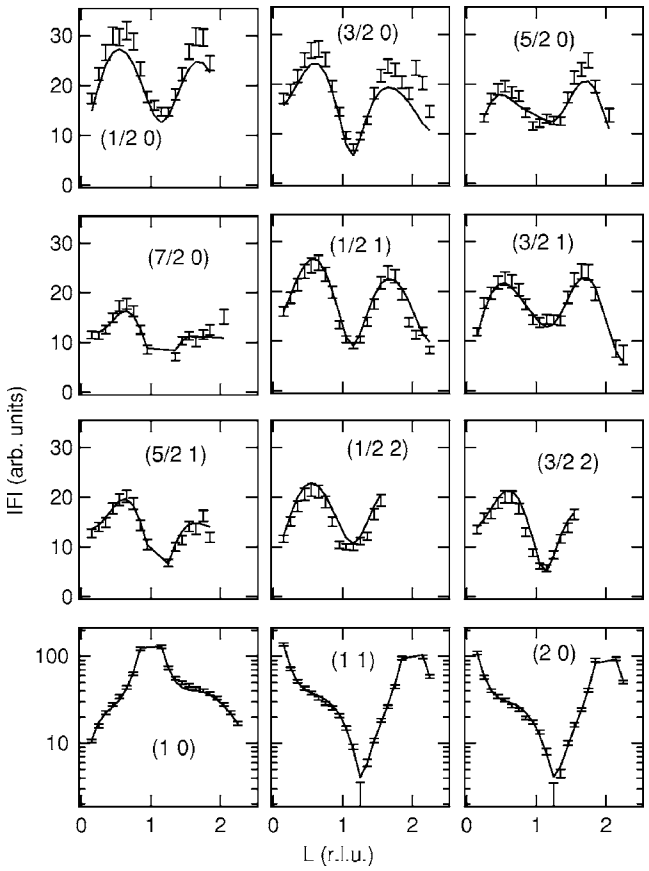

FIG. 2. Experimental structure factors and best fit for Pt(110)-(2×1)Mn-2D.

to j and it refers to the mean position of atomic sites in each layer. Best-fit values are reported in Table I. We find a strong contraction of the first interlayer distance ($\Delta d_{12}/d_{12}$ =−15%), but less pronounced than earlier values (−19%). Meanwhile, all other parameters are in quite good agreement with *ab initio* calculations,[22] with XRD,[23] and more particularly, with low-energy electron diffraction[24] LEED studies: b_3=0.19 Å (the "valley" site is closer to the surface than the buried one), p_2=0.04 Å, and p_4=0.033 Å.

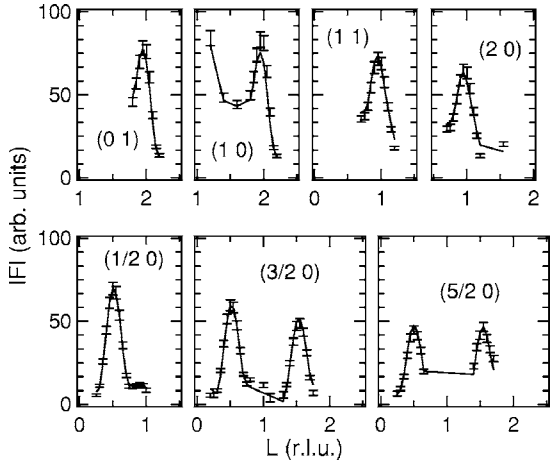

FIG. 3. Experimental structure factors and best fit for Pt(110)-(2×1)Mn-3D.

TABLE I. Clean Pt(110)-(1×2) results compared to previous studies. b_i and p_i denote the buckling and the pairing in layer i, respectively (see Fig. 4). d_{ij} is the interlayer spacing from layer i to j (reference is taken on the mean position in presence of buckling).

	XRD[a]	XRD[b]	LEED[c]	DFT[d]
b_3 (Å)		0.19±0.01	0.17	0.28
p_2 (Å)	0.05	0.040±0.005	0.04	0.04
p_4 (Å)	0.04	0.033±0.005	0.05	0.07
d_{12} (Å)	1.12	1.183±0.005	1.11	1.12
d_{23} (Å)	1.28	1.378±0.005	1.38	1.38
d_{34} (Å)		1.40±0.01	1.38	1.40
χ^2/R		4.5/0.05		

[a]Reference 23.
[b]This work.
[c]Reference 24.
[d]Reference 22.

2. Pt(110)-(1×2)Mn

The Pt(110)-(1×2)Mn model is illustrated in Fig. 4(a). Mn chains fill the empty rows, down the valleys (black atoms) and, consistent with the *p2mm* symmetry, they are assumed to reside in bulklike sites: as a consequence, the vertical height of Mn sites ($d_{\text{Mn-Pt}}$) is the only extra parameter with respect to the clean surface. The surface unit cell contains thus two nonequivalent sites, pure Mn and pure Pt, without random mixing, whereas all sites are assumed pure Pt for buried layers.

Several arguments point to an almost perfect complete top layer. Upon Mn deposition, we have no indication of a drastic reduction of the terrace and domain size which discards the possibility of massive long-range transport and of a mixture of PtMn alloy domains with uncovered Pt(110)-(1×2) domains. Moreover, the continuous increase of the intensity—versus coverage—leading to a maximum in the (111) reflection at about 0.5 ML is also a clear evidence of an almost perfect filling of the troughs, i.e., very few vacancies in the top layer and very few adatoms or small islands in the layer above. Finally, the rather good χ^2=3.6, together with an R factor of 0.08, assesses the quality of the ultimate model and is not compatible with a highly disordered surface. The experimental structure factors, their error bar, and the best fit are plotted in Fig. 1. The optimum parameters are reported in Table II.

The main result is the rippling of the top Pt-Mn layer: Mn adsorbs 0.19 Å above the Pt rows. In parallel, the presence of Mn in the missing rows entails a decrease in the buckling of layer 3, b_3=0.12 Å against 0.19 Å for the clean surface. In contrast, pairing and interlayer distances of Pt atoms are almost identical (d_{12}=1.16 Å, p_2=0.06 Å, and p_4=0.03 Å) with the exception of the second interlayer distance that is significantly larger (d_{23}=1.45 Å). The large rippling of the top layer may look surprising owing to the similar atomic radius of both species, but it has been clearly shown that the rippling is generally driven by the magnetic state of the elements entering the surface and not (only) by their size.[6,9] The present rippling is quite alike that derived from 2D NiMn

TABLE II. Structural parameters of surface MeMn(110) alloys (Me=Pt, Ni, or Cu). b_i, p_i, and d_{ij} denote the buckling, the pairing, and the interlayer spacing from layer i to j. $d_{\text{Mn-Me}}$ is the vertical spacing of Mn sites to the Pt (Ni, Cu) top layer. Mn is always shifted outward. $\langle D_{\text{Mn-NN}} \rangle$ is the mean nearest-neighbors distance of the Mn surface site calculated using the seven (relaxed) NN positions.

	Pt(110)[a]						Ni(110)[b] $c(2\times2)$	Cu(110)[c] $c(2\times2)$
	(1×2)		(2×1)-2D		(2×1)-3D			
(Å)	Expt.	Theor.	Expt.	Theor.	Expt.	Theor.	(XRD)	LEED
$d_{\text{Mn-Me}}$	0.19±0.03	0.19	0.16±0.02	0.12	0.19±0.06	0.16	0.30	0.22
b_3	0.12±0.01	0.14	0.026±0.006	0.11		0.04	0.036	0.01
p_2	0.060±0.005	0.11	0.017±0.004	0.03	0.022±0.006	0.03		
p_4	0.030±0.005		0.006±0.002					
d_{12}	1.16±0.01	1.06	1.16±0.01	1.14	1.19±0.04	1.15	1.13	1.20
d_{23}	1.45±0.01	1.58	1.443±0.006	1.52	1.45±0.04	1.48	1.254	1.29
d_{34}/d_{al}	1.40±0.01	1.37	1.374±0.003	1.38	1.36±0.01	1.33	1.242	1.27
d_{bulk}	1.3875	1.38	1.3875	1.38	1.3875	1.38	1.246	1.278
$\langle D_{\text{Mn-NN}} \rangle$	2.74±0.02	2.68	2.75±0.01	2.72	2.77±0.02	2.74		
χ^2/R	3.6/0.08		2.9/0.07		3.0/0.07		2.6/0.03	

[a]This work.
[b]Reference 10.
[c]Reference 9.

and CuMn surface alloys[6–10] [0.30 and 0.22 Å, respectively, for a (110) substrate] and somewhat larger than for a MnAg (0.07 Å) surface alloy.[25] Surface corrugation and pairing combine to give a unique distance between atoms in the top layer (Mn or Pt) and Pt in the second layer ($D_{\text{Mn-Pt}}$ =2.71±0.02 Å and $D_{\text{Pt-Pt}}$=2.713±0.008 Å). Note that Mn-Mn distances in the surface layer are comparatively quite large, being fixed by the substrate lattice at $D_{\text{Mn-Mn}}$ =2.775 Å. Another Mn nearest neighbor (NN) is located underneath in the third layer at an intermediate distance $D_{\text{Mn-Pt}}$=2.74±0.04 Å. These seven bonds combine to give an average distance $\langle D_{\text{Mn-NN}} \rangle$=2.74±0.02 Å.

In addition to structural parameters, we also optimized individual isotropic Debye parameters for the three outermost layers (B_1, B_2, B_3), an overall scale factor S, and a second scale factor $S2$ between noninteger rods and CTRs (Table III). For the surface layer, a unique Debye parameter was considered, the structural disorder overcoming the thermal contribution [associated also with some amount of chemical disorder (see below)]. B_1 and B_2 values double compared to bulk, but are comparable to that ones of clean Pt(110)-(1×2) (see also Ref. 23). It should be noted that anisotropic vibrations in the surface layer do not improve the fit.

Clean Pt and the (1×2)Mn surface, measured under identical experimental conditions, yield the same scale factor (S =0.43±0.01 and 0.433±0.005, respectively). In fact, $S2$ (=0.63) plays the role of the long-range order (LRO) parameter in bulk alloys and reveals the fraction of "wrong" atoms on each surface site. Using Warren's definition,[26] we conclude that each atomic site is occupied at 82% by "right" atoms. However, this amount is underestimated because well-ordered alloy domains with a short correlation length compared to the detector acceptance are not integrated in the fractional rods, which contribute to lower the $S2$ value.

3. Pt(110)-(2×1)Mn-2D

A very simple (2×1) 2D surface is shown in the top view of Fig. 4(b). It is made of alternating Mn and Pt atoms along the dense rows of an fcc(110) (nonreconstructed) surface. However, this model, as well as several others with Mn confined to the top layer, does not fit the experimental data and yields pretty high χ^2. A reasonable agreement (χ^2=2.9 and R=0.08) was reached only including, for the model of Fig. 4(b), Mn in subsurface layers. In fact, we find that buried Mn atoms reside almost exclusively in layer 3, just below the Pt surface site. This three-layer sandwich, PtMn/Pt/PtMn [side view of Fig. 4(b)], mimics the Pt_3Mn $L1_2$ bulk phase stacking. This arrangement served as a start model for the structure search, which was performed with the same structural parameters as above but for the pairing that symmetry allows, i.e., in the $[1\bar{1}0]$ direction instead of [001]. In addition, the Mn concentration was optimized in the three topmost layers, deeper ones being assumed to be pure Pt. A reverse stacking, with pure Pt at the surface and a mixed PtMn underlayer does not match the experimental data (χ^2=8.5). This can be understood intuitively by directly inspecting the structure factor data: a larger electron density in layer 1 than in layer 2 entails a bump between Bragg peaks in CTRs. Such a reverse segregation, with Pt at the surface, was observed on the Co/Pt(111) system [see the (10) rod in Fig. 4 of Ref. 27] but not in the present instance [Fig. 2, (11) and (20) rods].

The best fit is compared to experimental structure factors in Fig. 2 and the parameter values are reported in Table II

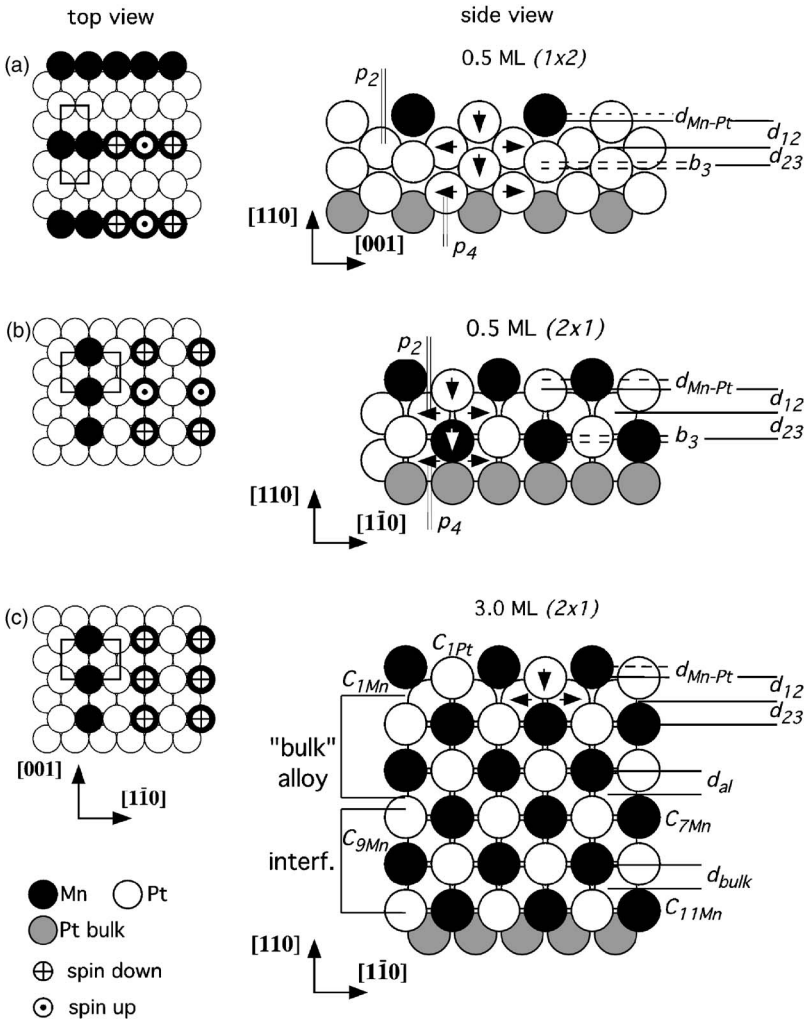

FIG. 4. Models for the three optimized structures: (a) Pt(110)-(1×2)Mn, (b) Pt(110)-(2×1)Mn-2D, and (c) Pt(110)-(2×1)Mn-3D. On the top view, the surface unit cell is shown and the magnetic order is sketched with arrows pointing up and down. Note that the AF ordering doubles the surface unit cell.

(displacements) and Table III (composition and Debye parameters). For the displacements, the picture is essentially the same as that of the (1×2) surface apart for the pairing direction. Albeit slightly less, the (2×1) top layer is rippled (0.16 Å), here again with Mn shifted out. The interlayer distances are almost the same (d_{12}=1.16 Å and d_{23}=1.44 Å), while buckling and pairing in deeper layers are much smaller (b_3=0.026 Å, p_2=0.017 Å, and p_4=0.006 Å). The latter differences are not surprising since lateral displacements are limited by the dense packing in the [1$\bar{1}$0] direction in con-

TABLE III. Nonstructural parameters for the three measured PtMn alloys. $C_{i\mathrm{Mn}}$ and $C_{i\mathrm{Pt}}$ represent the Pt concentration on the Mn and Pt sites, respectively, of layer *i*.

	Pt(110)-(1×2)Mn	Pt(110)-(2×1)Mn-2D	Pt(110)-(2×1)Mn-3D
B_1 (Å^2)	0.8±0.2	0.43±0.06	0.31(Pt)/0.44(Mn)
B_2 (Å^2)	0.7±0.1	0.31(Pt)/0.44(Mn)	0.31(Pt)/0.44(Mn)
B_3 (Å^2)	0.4±0.1	0.31(Pt)/0.44(Mn)	0.31(Pt)/0.44(Mn)
B_{bulk} (Å^2)	0.31	0.31	0.31
$C_{1\mathrm{Pt}}$ (at. % Pt)	82±5[a]	80±4	90±10[a]
$C_{1\mathrm{Mn}}$ (at. % Pt)	18±5[a]	5±13	10±10[a]
C_2/C_{2n} (at. % Pt)		96±4	92±8[b]
$C_{3\mathrm{Pt}}$ (at. % Pt)		100	90±10[a]
$C_{3\mathrm{Mn}}$ (at. % Pt)		70±4	10±10[a]
*S*2	0.63±0.02		0.80±0.02

[a]Derived from *S*2.
[b]Derived from *S*2 and *SN*=0.94.

trast with the [001] direction for the first structure. For this surface structure, the four Mn NN in layer 2 are at $D_{\text{Mn-Pt}}=2.73\pm0.01$ Å, a bit larger compared to the previous surface, owing essentially to the absence of pairing. The NN from layer 3 is at $D_{\text{Mn-Pt}}=2.75\pm0.02$ Å. The seven Mn–Pt bonds combine to give an average distance $\langle D_{\text{Mn-Pt}}\rangle=2.75\pm0.01$ Å, larger by 0.01 Å compared to the previous situation.

A single LRO parameter cannot be defined in this case, so that the atomic composition was fitted for each site within the first three layers (Table III). The surface layer is paved with a regular distribution of Pt-rich and Mn-rich sites ($C_{1\text{Pt}}=80$ at. % and $C_{1\text{Mn}}=5$ at. % Pt) and the second layer is almost pure Pt. As explained above, the third layer cell contains a pure Pt site and a mixed Pt-Mn site ($C_{3\text{Mn}}=70$ at. % Pt): mixing Mn and Pt on the former site results in a worsening of χ^2 so that the site was kept pure Pt. The total amount of Mn in the surface region, 0.77 ± 0.14 ML, is a little larger than the 0.62 ML estimated by the evaporation rate calibration. A unique Debye parameter was fitted ($B_1=0.43$ Å^2) for all atoms in layer 1—surprisingly, unphysical values are obtained for independent Pt and Mn Debye parameters. For deeper layers, we assigned bulk values to each species ($B_{\text{Pt}}=0.31$ and $B_{\text{Mn}}=0.44$ Å^2). Leaving them free does not improve the agreement and, anyhow, our structural parameters are very weakly sensitive to Debye parameters.

4. Pt(110)-(2×1)Mn-3D

For the alloy obtained by annealing the 3 ML film, too many atomic sites are involved to be treated independently. So, for the calculations, the crystal was separated in four distinct regions from surface to bulk [Fig. 4(c)]: (a) a mixed PtMn surface layer, similar to the previous one; (b) a five-layer thick $Pt_3Mn(110)$ slab with $L1_2$ structure and interlayer distance d_{al}; (c) a five-layer thick diffuse interface alternating mixed Pt-Mn and Pt layers (in the mixed layers, one site is pure Pt and the other is a variable mixture of Pt and Mn; the interlayer distance is d_{al} for layers 7 and 8 and d_{bulk} for deeper layers); and (d) bulk.

All odd layers [in regions (a) and (b)] contain one Pt site and one Mn site, while all even layers are assumed pure Pt. This hypothesis will be relaxed below. The first two spacings d_{12} and d_{23}, the corrugation $d_{\text{Mn-Pt}}$ in layer 1, the pairing p_2 in layer 2, and the interlayer distance d_{al} were optimized. Within the error bars, the surface structure is similar to that of the thin (2×1) alloy (Table II), with Mn atoms shifted 0.19 Å above the top layer.

For the Pt_3Mn-like slab, the interlayer spacing $d_{i,i+1}$ was assumed equal to d_{al} for $i=2-7$. The optimized distance, 1.36 Å, i.e., ~2% smaller than the Pt spacing, yields a unit cell volume of ~59.24 Å^3 (using the Pt in-plane lattice), in good agreement with Pt_3Mn bulk value (59.32 Å^3). Surface Mn atoms have four NN at 2.76 ± 0.02 Å, one at $D_{\text{Mn-Pt}}=2.78\pm0.04$ Å, and two in the surface plane at $D_{\text{Mn-Pt}}=2.775$ Å. The average distance $\langle D_{\text{Mn-Pt}}\rangle$ is 2.77 ± 0.02 Å, which is the largest one found in the PtMn surface alloys.

In the diffuse interface, the Pt concentration of the Mn site in mixed layers (=0% Pt in the Pt_3Mn region above) increases monotonously: $C_{7\text{Mn}}=20$ at. % Pt, $C_{9\text{Mn}}=62$ at. % Pt, and $C_{11\text{Mn}}=83$ at. % Pt. As expected, this is not an abrupt interface. In total, 2.2 ML Mn are distributed over the 11 layers entering the calculations, i.e., less than the 3 ML estimated at the beginning, pointing to possible diffusion in more than 11 layers. The Debye-Waller factors were kept fixed at bulk values, and two extra parameters, an overall scale factor and the scale factor $S2$, were fitted from which we extract the intralayer chemical order. The optimum structure factors are displayed in Fig. 3.

The second scale factor ($S2$) plays the role of an intralayer order parameter. However, the presence of domain walls needs to be considered. As mentioned above, alloy domains extend over 6 nm on the average parallel to the surface (the overall thickness being about 1.5 nm) so that, with the slit aperture used for recording, ~30% of the superstructure rods intensity is lost. After correction, we find $S2=0.8$, which corresponds to a 90% fraction of each site occupied by the right species, i.e., 10% Pt on Mn site in regions (a) and (b). The surface structure resembles that of the (2×1) 2D film both for the composition and the chemical order, and for the atomic positions.

The data set collected for this latter surface is smaller than in the former cases. Moreover, mainly reflection characteristics of the $L1_2$ phase were recorded and CTRs were only partially measured (Fig. 3): in other words, we lack some parts of the spectra to properly extract the scale factor. Indeed, the measurement of CTRs close to Bragg peaks is essential for evaluating the actual intensity of superstructure reflections. In fact, the absolute scale for this (2×1) 3D structure is known from the previous structural experiment—(2×1) 2D—as both were performed in exactly the same conditions. The normalization factor between the two experiments, $SN=0.94$, gives a measurement of the order parameter for the chemical contrast along (110) in the $L1_2$ phase. Generalizing Warren's expression to the case of three atomic sites is then possible, from the values of SN and $S2$, to find the Pt concentration of even layers in region (b) $C_{2n}=92\%$.

III. THEORETICAL CALCULATIONS

A. Method

For the *ab initio* calculations, we use density-functional theory as employed in the full-potential linearized augmented plane-wave (FLAPW) method.[28] The applicability of this method to determine multilayer relaxations has been demonstrated for the missing row reconstruction of Pt(110) in a previous paper.[22] In Table I, we compare once more these results to the experimental data: as can be seen, on average the experimental and theoretical results for the relaxations differ only by about 0.03 Å.

The accurate description of the structure of 3*d* metals on 5*d* substrates in density-functional theory is a nontrivial problem: while the 3*d* metals are normally better described within the generalized gradient approximation (GGA), the lattice constants of the members of the 5*d* series are well reproduced in the local-density approximation (LDA). While GGA overestimates the lattice constant of Pt by 1.7%, in

TABLE IV. Calculated magnetic moment (μ), total energy (E_{tot}), and energy difference between F and AF orderings [E(AF−F)]. The value of μ is relative to Mn surface atoms. Energies are given per Mn atom and they are referenced to the AF (2×1) surface alloy. For the 3D-alloy calculation, AF means antiferromagnetic coupling within and between the layers. The experimental μ value for Pt_3Mn is also reported.

	(1×2)		(2×1)-2D		(2×1)-3D		$c(2\times2)$		Pt_3Mn[a]
	F	AF	F	AF	F	AF	F	AF	F
μ (bohr)	3.94	3.88	3.99	3.99	4.02	4.02	4.02	3.99	3.64
E_{tot} (meV)	267	139	13	0			51	65	
E(AF−F) (meV)	−128		−13		66		14		

[a]Reference 11.

LDA it is only 0.4% too small.[22] On the other hand, LDA underestimates structural parameters of 3*d* metals typically by 2% or 3%. Furthermore, there is evidence that LDA tends to underestimate the magnetism of Mn.[29] Our calculations of Mn on Pt(110) clearly reflect these difficulties: e.g., the experimentally observed buckling of the Mn/Pt surface layer (between 0.16 and 0.19 Å) can be reproduced neither by LDA nor by GGA. In LDA, all investigated overlayer geometries [(2×1), (1×2), and $c(2\times2)$] show almost no corrugation at all. In GGA calculations, the magnetic moment of Mn is increased by about 0.3 μ_B, followed by an increase of atomic volume of Mn. However, the over expanded Pt substrate reduces this effect again, and the corrugations remain in the order of 0.03–0.08 Å, i.e., at most half the experimental value. A typically applied solution to this problem to keep the Pt substrate atoms at their ideal bulk positions using the experimental lattice constant and to relax only the positions of the Mn atoms is not applicable in our case, where large multilayer relaxations are observed.

Therefore, we have chosen an alternative approach to treat the Pt atoms [i.e., the spherical regions around the Pt sites, the so-called muffin-tin (MT) spheres] in the LDA, but to apply gradient corrections to the Mn atoms and the region in between the MT spheres (interstitial region). Since in the FLAPW method the MT spheres are nonoverlapping, this procedure is well defined. Performing test calculations for bulk Pt showed that in this way, the LDA lattice constant is almost reproduced and even a slightly better agreement with experiment (−0.3% of the experimental value) is obtained. Therefore, we used the approximation by Perdew *et al.*[30] as GGA, but with all gradient terms set to zero within the Pt MT spheres. In this way, the Mn moments were almost conserved at their GGA values and a realistic Pt in-plane lattice constant could be used for the multilayer relaxations. In our calculations, we used 11-layer films embedded in semi-infinite vacuum.

The muffin-tin radii were chosen to be 2.41 a.u. for Pt and 2.30 a.u. for Mn. We used a plane-wave cutoff of 4.0 $(\text{a.u.})^{-1}$ corresponding to about 130 basis functions per atom. The Brillouin zone was sampled with 12 $\mathbf{k}_\parallel$ points in the irreducible wedge for the calculations with two atoms in the in-plane unit cell and six $\mathbf{k}_\parallel$ points for the geometries with four atoms per layer.

The calculations were performed for three different surface alloys with (1×2), (2×1), and $c(2\times2)$ symmetries, with Mn confined to the surface layer. The (1×2) and (2×1) surfaces correspond to the superficial structures observed during this work. The hypothetical $c(2\times2)$ symmetry, never observed in the present study, corresponds to the situation of our previous studies of Cu(110)-$c(2\times2)$Mn (Ref. 9) and of Ni(110)-$c(2\times2)$.[10] Finally, calculations were made for a thick Pt_3Mn alloy film, which corresponds to the $L1_2$ phase [Fig. 4(c)]: Mn is arranged like in the surface (2×1) superstructure and is located below surface Pt and Mn in the third and fifth layers, respectively. This film corresponds roughly to the (2×1) 3D alloy studied in XRD, its thickness being that one of regions (a)+(b) defined in the previous paragraph.

Positions of atoms in the first three layers were allowed to relax. Comparison with calculations in which relaxation of all the layers is allowed showed that this changes the positions by less than 0.02 Å and the total energy not more than 6 meV.

B. Results

In Table IV, the energy of the films per Mn atom is reported for the three surface alloys and the bulklike alloy film. Among the surface alloys, the (2×1) superstructure is the ground state. The (1×2) is a metastable state frozen in at room temperature. It is interesting to remark that the $c(2\times2)$ superstructure, which is the ground state for Mn/Ni(110) and Mn/Cu(110) 2D alloys, has an intermediate energy. In the (2×1) 2D surface, the coupling is antiferromagnetic (AF). However, the energy difference E(AF-F) is small and for the thicker alloy the coupling at the surface is ferromagnetic (F). Instead, the (1×2) surface is clearly antiferromagnetic. The magnetic structure for the (2×1) and (1×2) AF cases is sketched in Fig. 4 with arrows pointing up or down. Note that the AF ordering doubles the surface mesh with respect to the period given by the chemical order.

For the thicker (3D) alloy, several magnetic structures are possible. Both within and between the PtMn layers, F and AF orders are possible. We investigated all variants of in-plane ferromagnetic order and found that the F-ordered surface layer likes to couple AF to a F ordered bulk alloy below. In-plane AF order at the surface cannot lower the total energy further and in-plane AF order in deeper layers leads to an even larger increase in total energy (cf. Table IV). We

TABLE V. Values of μ and r_{Mn} calculated for several MeMn surface alloys [$r_{Mn}=\langle D_{Mn\text{-}NN}\rangle-(a_{bulk}/\sqrt{2})/2$].

	Pt(110) (This work)			Pt(100)[a] Ref. 14	Cu(110) Ref. 9	Cu(100) Ref. 6	Cu(100) Ref. 33	Ag(100)[b] Ref. 35	Ni(100)[a] Ref. 34
	(1×2)	(2×1) 2D	(2×1) 3D	$c(2\times2)$	$c(2\times2)$	$c(2\times2)$	$c(2\times2)$	$c(2\times2)$	$c(2\times2)$
r_{Mn} (Å)	1.30	1.33	1.35	1.40	1.28	1.32	1.36	1.45	
μ (bohr)	3.88	3.99	4.02	4.1	3.82	3.75	4.09	4.15	3.5

[a]Calculated using the experimental lattice constant.
[b]Calculated using nonrelaxed bulk atomic positions.

note, however, that the three most stable magnetic configurations are separated by only 9 meV and the considered magnetic configurations form a rather dense spectrum of states, so that at room temperature several magnetic structures could be populated.

The magnetic moment per Mn surface atom is also reported in Table IV. A value of about 3.9 and 4 μ_B is obtained for (1×2) and (2×1), respectively, independent of the magnetic coupling. This value is even a little larger than the calculated one for NiMn and CuMn 2D surface alloys (Table V). In the third and fifth layers of the alloy, a moment of 3.77 μ_B is calculated, close to the value of 3.64 μ_B calculated for a thick Pt_3Mn layer of $L1_2$ phase.[13] The structural parameters calculated for the three models are reported in Table II. The magnetic structure does not influence much the interlayer relaxations [except for $d_{Mn\text{-}Pt}$ in the (1×2) structure], the variation being smaller than the experimental error bars. Values reported are for the ground magnetic state.

General trends observed in the experiment are well reproduced by theory, with some discrepancies in the numerical values. The rippling $d_{Mn\text{-}Pt}$ is quite well predicted both for (1×2) (0.19 Å for both experiment and theory) and (2×1) (0.16 and 0.12 Å, respectively). The trend observed in the interlayer distances, with a strong contraction of d_{12} and an expansion of d_{23}, is reproduced but amplified in the calculation. For the (1×2) phase, a d_{12} (d_{23}) value of 1.16 Å (1.45 Å) and 1.06 Å (1.58 Å) is obtained from experiment and calculation, respectively.

The major discrepancy is observed for the third layer buckling of the (2×1) 2D structure (0.026 Å in experiment and 0.11 Å calculated). This discrepancy doubtlessly follows from the hypothesis made of Mn confinement in the top layer solely. Comparison of columns 4 and 6 of Table II indicate that the calculated values can be strongly affected by the Mn content in layer 3, and in parallel, we note precisely that the buckling calculated for the 3D film (0.04 Å) as well as the surface corrugation (0.16 Å) are much closer to experimental results for the 2D alloy. This points to the presence of Mn in the third layer of the (2×1) alloy—as clearly indicated by XRD—while for the (1×2) structure the introduction of Mn in deeper layers worsens the agreement between experimentally and theoretically determined relaxations. This supports the picture that Mn diffusion into deeper layers occurs only during the annealing process which leads to the formation of the (2×1) structure.

IV. DISCUSSION

From a structure and composition point of view, there are many similarities between Mn/Pt(110) surface alloys and those formed by Mn deposition on other (110) surfaces, such as Cu (Ref. 9) and Ni (Ref. 10): they all form a mixed and rippled MeMn top layer (Me=Cu, Ni, or Pt) with Mn sitting between 0.16 and 0.3 Å above the metal sublattice, irrespective of the metal atomic radius; second, there is a strong contraction of the first interlayer spacing, characteristic of most clean (110) fcc faces of transition metals and bimetallic alloys; third, the second layer spacing is weakly expanded [also typical of (110) fcc samples]; and finally, the third layer exhibits a weak buckling. Part of these features are present at the (100) face of the same Cu (Ref. 8) and Ni (Ref. 7) metals.

The main, marked, difference between Cu and Ni on the one hand and Pt on the other hand, upon Mn evaporation, resides in the occurrence of $c(2\times2)$ pattern in the former ones and (1×2) or (2×1) patterns in the latter. This difference, no doubt, follows from the change in the lattice parameter, roughly 10% larger for Pt than for Cu and Ni, and from the trend of Mn atoms to be surrounded by the other species and to occupy a large volume.

The NN distance of (fcc) γ-Mn at room temperature is $D_{Mn\text{-}Mn}=2.64$ Å, when extrapolated from temperatures above 1095 °C.[31] A large Mn-Mn distance ($D_{Mn\text{-}Mn}=2.92$ Å) is found in the Cu(100)-$c(8\times2)$Mn structure, where Mn forms a dense, pseudohexagonal layer above the substrate.[32]

In Ni and Cu surface alloys with (100) orientation, the NN distance (2.492 and 2.556 Å, respectively) is too short for allowing Mn-Mn pairs, and the stable phase is a $c(2\times2)$ order with a checkerboard arrangement of the two kinds of atoms. Anyhow, steric considerations alone do not explain the structure of MeMn surface alloys, and interactions with the shell of next neighbors also play an important role. The (110) face of both Ni and Cu shows also a $c(2\times2)$ superstructure with the same kind of atomic arrangement. In this case, however, the Ni(110) (Cu) inter-row spacing, 3.524 Å (3.615 Å), is the same as the Mn-Mn distance in the $c(2\times2)$ reconstruction on (100) face. Repulsion between Mn seems to play a role in the equilibrium structure, avoiding the growth of a (2×1) structure: Ni (Cu) atoms occupy both the NN and the next-nearest-neighbor (NNN) shells around Mn, which results in a Mn-Mn spacing of 4.316 Å (4.427 Å), for the closest pairs.

On Pt(110), the situation is quite different, both for the presence of the missing row reconstruction and for the larger inter-row spacing (3.924 Å). The former allows the growth of the metastable (1×2) arrangement with a dense stacking of Mn, in the troughs, along the $[1\bar{1}0]$ direction, in spite of a very unfavorable total energy (Table IV). Upon annealing, NNN interactions favor the growth of the (2×1) phase, formed by alternating Mn and Pt along the surface rows as in the $c(2\times2)$ case, but with atoms of the same kind aligned in the [001] direction (Fig. 4). This is exactly the atomic disposition in mixed (110) planes of Pt_3Mn phase.

Summarizing the theoretical results for MeMn surface alloys (with Mn in the top layer only), it can clearly be seen that chemical ordering, volume of Mn (and hence its magnetic moment, as discussed below), and magnetic ordering are related:

(a) F order is predicted for the $c(2\times2)$ structure on Cu(100),[8] and it seems probable for the $c(2\times2)$ structure on Cu(110).[9]

(b) F order is calculated for the Pt(110)-$c(2\times2)$Mn phase (not observed experimentally).

(c) AF order is the fundamental state of Pt(110)-(1×2)Mn surface, with large (negative) $E(\mathrm{AF}-\mathrm{F})$.

(d) AF order is also calculated for Pt(110)-(2×1)Mn, but $E(\mathrm{AF}-\mathrm{F})$ is one order of magnitude smaller than in the (1×2) surface alloy.

Therefore, schematizing these results: the ground state is F when the occurrence of $c(2\times2)$ is observed, i.e., Mn is surrounded by the other species only; if (1×2) or (2×1) structures occur—which results in Mn sites having two in-plane Mn neighbors—the order is AF. We note that for the (2×1) surface, the AF order is favored, despite the large Mn-Mn distance.

The DFT results are a little more complex for the 3D alloy, modeled by a film with a Pt_3Mn-like structure. In the third and fifth layer, Mn is surrounded by Pt only and a cut through the surface showing the (001) plane [side view of Fig. 4(c)] reveals that, on this face, the $L1_2$ phase corresponds to the $c(2\times2)$ order. It is worth then to remember that our DFT calculations favor F order within each buried layer and F coupling between them, as in bulk Pt_3Mn.[11] The order within surface atoms is also F, but AF coupling with the buried layers is predicted. It is interesting to compare with the theoretical results for the Pt(100) face.[14] Calculations performed for a the three-layer-thick slab of Pt_3Mn-like surface alloy [PtMn/Pt/PtMn/Pt(100)] show the same kind of fundamental state, with F order within each one of the two magnetic layers and AF coupling between them.

There is a significant increase in the magnetic moment from the (1×2) to the (2×1) surface alloys, i.e., switching from pure to mixed dense row in the top layer. The magnetic moment reaches about 4 μ_B for the latter structure. The key parameters for large moments are the number and the type of NN and the size of Mn atoms. In the $L1_2$ phase, Mn is surrounded by 12 NN as opposed to 7 for the surface site of the PtMn structures considered here, (1×2), (2×1), and $c(2\times2)$. Both in Pt_3Mn and in these surface alloys, all Mn NN are Pt atoms, except in the (1×2) structure where two of them are Mn. The $c(2\times2)$ derives from the (2×1) by a simple shift of every other dense row.

The situation is different on the Me(100) face as each atom has eight NN, four of which in the surface plane. This favors the $c(2\times2)$ symmetry, which only avoids Mn–Mn bonds and results in F ordering, as confirmed by both experimental and theoretical results for Cu(100).

However, the nature and number of NN do not fully explain the magnetic order, as clearly shown by our results for the (2×1) and $c(2\times2)$ arrangements. The local geometry around Mn is indeed the same, but the magnetic order is AF for the former structure and F for the latter one. In the (2×1), two Mn atoms belong to the second shell of Mn neighbors, whereas for the $c(2\times2)$ configuration, the closest Mn are in the third shell.

The comparison with Cu(100)-$c(2\times2)$Mn and with bulk Pt_3Mn helps to clarify the case. The (110) is a low density face, and Mn has only two NN in the surface plane of Pt(110)-(1×2)Mn, which leaves space for the interaction between Mn atoms at 3.924 Å. This is responsible for the AF order. In the two cases cited above, Mn is completely surrounded by the other metal. In such a frame, it is not surprising that Kim *et al.*[14] found F order within the top layer of their (three layer thick) Pt(100)-$c(2\times2)$Mn surface alloy.

The size effect on Mn magnetic moment can be quantified by means of an "average radius" $r_{\mathrm{Mn}}=\langle D_{\mathrm{Mn\text{-}NN}}\rangle-(a_{bulk}/\sqrt{2})/2$. This allows the comparison with findings for Mn alloys on different (fcc) substrates. In Table V, the ground-state magnetic moments of surface Mn atoms calculated in the present work are reported, together with those obtained for $c(2\times2)$ alloys formed on the (100) and (110) surfaces of Cu,[6,9,33] Ni,[34] Pt,[14] and Ag,[35] and with the respective r_{Mn} values. The radii are calculated from the optimized atomic positions and using the lattice constant determined by the theory. In the case of Ag(100) and Pt(100), the values are obtained for alloys two and three layers thick, respectively. For Ag, the moment was calculated keeping atoms at the bulk position. Two different values of radius and magnetic moment are available for Cu(100)-$c(2\times2)$Mn from different theoretical approaches that yield a different lattice constant. Figure 5 shows a plot of μ versus r_{Mn} from Table V. Results for (110) and (100) face are shown with diamonds and squares, respectively. Experimental values of Pt_3Mn and Ni_3Mn alloys are also reported (the radius is calculated using a_{Pt} and a_{Ni}, respectively).

We see that, for the two orientations, the moment increases almost linearly with the size until it reaches a value of ~4 μ_B. The general trend indicates quite clearly that one must favor large atomic-size metals in order to increase the magnetic moment and to approach the atomic value. In parallel, more open surfaces—the (110) with respect to the (100)—yield larger moments for similar atomic volume.

Measuring the magnetic properties of AF surfaces is a difficult task. Measurements were performed in the past for the cases where ferromagnetism is expected. The magnetic properties of Cu(100)-$c(2\times2)$Mn and Ni(100)-$c(2\times2)$Mn were investigated by x-ray absorption spectroscopy and x-ray magnetic circular dichroism (XMCD) at the Mn $L_{2,3}$

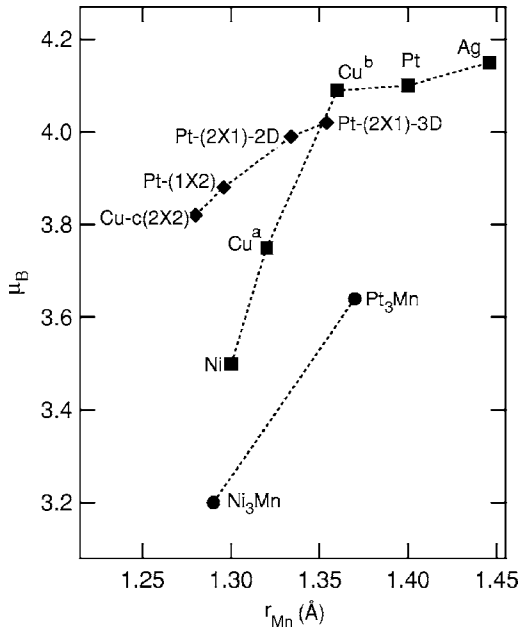

FIG. 5. Magnetic moments of surface Mn atoms versus r_{Mn} (see Table V). Diamonds are for (110) surfaces. Squares represent Me(100)-$c(2\times2)$Mn surface alloys. Cu^a and Cu^b are the value calculated in Refs. 6 and 33, respectively, for the same surface. Experimental values for Ni_3Mn and Pt_3Mn alloys are also given (circles). The experimental r_{Mn} values for (1×2) and (2×1)-2D surfaces are 1.35±0.02 and 1.36±0.01 Å, respectively.

edge.[36] This study showed that, in both cases, Mn is in a high spin state. Only the NiMn surface exhibits a magnetic ordering at room temperature, the coupling being entirely F, with the Mn moment aligned parallel to the substrate magnetization, whereas in bulk NiMn the spin alignment is AF on both the Mn and Ni sublattices. In the CuMn surface, the magnetic order appears only at low temperature, as shown more recently by XMCD performed at $T<50$ K.[37]

V. SUMMARY

Three different surface alloys obtained by deposition of Mn on Pt(110)-(1×2) were studied quantitatively. Evaporation of about 3 ML, followed by annealing at 790 K, results in an epitaxial ~1.5-nm-thick $L1_2$ phase of composition close to Pt_3Mn. As the film grows in epitaxy on the Pt(110) substrate, it is strained in-plane and compressed along the growing direction, yielding roughly the unit volume of the corresponding bulk alloy. An analogous result was found by Gallego *et al.*,[12] who grew a bulklike $Pt_3Mn(111)$ slab. However, in contrast with the mixed PtMn termination of the present surface, their film was Pt terminated. This is not surprising because it is well know that segregation reversal happens at the (110) surface of several Pt-based alloys, with respect to their (111) face.[38] Deposition of about 0.5 ML on the substrate at 560 K, yields a 2D alloy with (2×1) symmetry, and atoms arranged like in mixed $Pt_3Mn(110)$ planes. Some amount of Mn was found in the third layer, below the surface Pt site (as expected in a $L1_2$ phase). During deposition, long-range ordering takes place above a critical thickness of about 0.37 ML, in close analogy with the Ni(110)-$c(2\times2)$Mn case, where the critical thickness was 0.35 ML.[10]

Upon deposition of 0.5 ML at room temperature, a metastable (1×2) structure forms, which is explained by Mn filling essentially the Pt(110)-(1×2) troughs. The superstructure is observed up to 1 ML coverage. Both the (1×2) and (2×1) surface alloys show a large rippling, with Mn shifted outward by 0.19 and 0.16 Å, respectively, as already observed for several Mn-based $c(2\times2)$ surface alloys.

Theoretical calculations were then performed for three ideal surface alloys with Mn in the top layer and (1×2), (2×1), and $c(2\times2)$ symmetries, respectively. Among them, the (2×1) is the ground state, as confirmed by the experimental results.

There is good agreement between DFT and XRD, the tendencies observed experimentally being reproduced for all the structural parameters. Some of the numerical values are correctly predicted, in particular, for the surface corrugation. The strong contraction of the first interlayer spacing followed by an oscillation of the distance in the deeper layers, observed for the Mn/Pt(110) alloys, is a characteristic of fcc (110) metal faces.

Calculations point to an antiferromagnetic ground state for the (1×2) structure. The (2×1) alloy is AF too, but the ferromagnetic state is much closer in energy. Finally, a thick alloy film with $L1_2$ symmetry was considered, with Mn in the first, third, and fifth layers. We find a ferromagnetic order within each layer and an antiferromagnetic coupling between the top layer and the buried ones.

The calculated magnetic moment of surface Mn atoms is very large, ranging between 3.9 and 4 μ_B. This is associated with the large surface rippling, which balances the general trend to shorten the substrate-adsorbate NN distance, compared to what is expected on the basis of the sum of the atomic radii. The net result is a large Mn atomic volume, characteristic that is common to all Mn-based surface alloys. The effect on the magnetic properties is amplified by the (110) orientation, which implies only two NN in the surface plane.

ACKNOWLEDGMENTS

Beam time at ESRF is acknowledged. The authors would like to thank the BM32 beam line staff for technical support. V.L. thanks the Spanish Ministry of Education and Science (MEyC) for its support through the "Ramon y Cajal" program.

*Corresponding author. Electronic address: maurizio.de-santis@grenoble.cnrs.fr

[1] F. J. Himpsel, J. E. Ortega, G. J. Mankey, and R. F. Willis, Adv. Phys. **47**, 511 (1998).
[2] P. Gambardella, M. Blanc, H. Brune, K. Kuhnke, and K. Kern, Phys. Rev. B **61**, 2254 (2000).
[3] Y. Garreau, A. Coati, A. Zobelli, and J. Creuze, Phys. Rev. Lett. **91**, 116101 (2003).
[4] P. Gambardella, A. Dallmeyer, K. Malti, M. C. Malagoli, W. Eberhardt, K. Kern, and C. Carbone, Nature (London) **416**, 301 (2002).
[5] Y. Gauthier, M. Schmid, S. Padovani, E. Lundgren, V. Bus, G. Kresse, J. Redinger, and P. Varga, Phys. Rev. Lett. **87**, 36103 (2001).
[6] M. Wuttig, Y. Gauthier, and S. Blügel, Phys. Rev. Lett. **70**, 3619 (1993).
[7] M. Wuttig, T. Flores, and C. C. Knight, Phys. Rev. B **48**, 12082 (1993).
[8] M. Wuttig, C. C. Knight, T. Flores, and Y. Gauthier, Surf. Sci. **292**, 189 (1993).
[9] C. Ross, B. Schirmer, M. Wuttig, Y. Gauthier, G. Bihlmayer, and S. Blügel, Phys. Rev. B **57**, 2607 (1998).
[10] M. De Santis, V. Abad-Langlais, Y. Gauthier, and P. Dolle, Phys. Rev. B **69**, 115430 (2004).
[11] B. Antonini, F. Lucari, F. Menzinger, and A. Paoletti, Phys. Rev. **187**, 611 (1969).
[12] S. Gallego, C. Ocal, J. Méndez, X. Torrelles, and F. Soria, Surf. Sci. **482-485**, 1303 (2001).
[13] S. Gallego, C. Ocal, M. C. Muñoz, and F. Soria, Phys. Rev. B **56**, 12139 (1997).
[14] W. Kim, S. C. Hong, J. Seo, S.-J. Oh, H. G. Min, and J.-S. Kim, Phys. Rev. B **70**, 174453 (2004).
[15] T. Sato, M. Tsunoda, and M. Takahasci, J. Magn. Magn. Mater. **240**, 277 (2002).
[16] R. Baudoing-Savois, G. Renaud, M. De Santis, A. Barbier, O. Robach, P. Taunier, P. Jeantet, O. Ulrich, J. P. Roux, M. C. Saint-Lager, A. Barski, O. Geaymond, G. Berard, P. Dolle, M. Noblet, and A. Mougin, Nucl. Instrum. Methods Phys. Res. B **149**, 213 (1999).
[17] E. Vlieg, J. F. Van Der Veen, S. J. Gurman, C. Norris, and J. E. Macdonald, Surf. Sci. **210**, 301 (1989).
[18] R. Feidenhans'l, Surf. Sci. Rep. **10**, 105 (1989).
[19] I. K. Robinson, in *Handbook on Synchrotron Radiation*, edited by G. S. Brown and D. E. Moncton (North-Holland, Amsterdam, 1991), Vol. 3, p. 221.
[20] E. Vlieg, J. Appl. Crystallogr. **30**, 532 (1997).
[21] E. Vlieg, J. Appl. Crystallogr. **33**, 401 (2000).
[22] S. Baud, C. Ramseyer, G. Bihlmayer, S. Blügel, C. Barreteau, M. C. Desjonquères, D. Spanjaard, and N. Bernstein, Phys. Rev. B **70**, 235423 (2004).
[23] E. Vlieg, I. K. Robinson, and K. Kern, Surf. Sci. **233**, 248 (1990).
[24] P. Fery, W. Moritz, and D. Wolf, Phys. Rev. B **38**, 7275 (1988).
[25] P. Schieffer, C. Krembel, M.-C. Hanf, G. Gewinner, and Y. Gauthier, Phys. Rev. B **62**, 2944 (2000).
[26] B. E. Warren, *X-Ray Diffraction* (Dover, New York, 1990), Chap. 12, p. 208.
[27] M. De Santis, R. Baudoing-Savois, P. Dolle, and M. C. Saint-Lager, Phys. Rev. B **66**, 085412 (2002).
[28] E. Wimmer, H. Krakauer, M. Weinert, and A. J. Freeman, Phys. Rev. B **24**, 864 (1981).
[29] T. Asada and S. Blügel, Physica B **237–238**, 359 (1997).
[30] J. P. Perdew, J. A. Chevary, S. H. Vosko, K. A. Jackson, M. R. Pedersen, D. J. Singh, and C. Fiolhais, Phys. Rev. B **46**, 6671 (1992).
[31] D. Tian, S. C. Wu, F. Jona, and P. M. Marcus, Solid State Commun. **70**, 199 (1989).
[32] Y. Gauthier, M. Poensgen, and M. Wuttig, Surf. Sci. **303**, 36 (1994).
[33] M. Eder, J. Hafner, and E. G. Moroni, Phys. Rev. B **61**, 11492 (2000).
[34] O. Rader, W. Gudat, C. Carbone, E. Vescovo, S. Blügel, R. Kläsges, W. Eberhardt, M. Wuttig, J. Redinger, and F. J. Himpsel, Phys. Rev. B **55**, 5404 (1997).
[35] O. Elmouhssine, G. Moraïtis, J. C. Parlebas, C. Demangeat, P. Schieffer, M. C. Hanf, C. Krembel, and G. Gewinner, J. Appl. Phys. **83**, 7013 (1998).
[36] W. L. O'Brien and B. P. Tonner, Phys. Rev. B **51**, 617 (1995).
[37] Y. Huttel, C. M. Teodorescu, F. Bertran, and G. Krill, Phys. Rev. B **64**, 094405 (2001).
[38] Y. Gauthier, Surf. Rev. Lett. **3**, 1663 (1996).